THRESHOLD IDENTIFICATION FOR MICRO-TOMOGRAPHIC DAMAGE CHARACTERIZATION IN A SHORT FIBRE REINFORCED POLYMER

SCHOLARONE™
Manuscripts

1
2
3
4
5
6
7
8
9
10
11
12
13
14
15
16
17
18
19
20
21
22
23
24
25
26
27
28
29
30
31
32
33
34
35
36
37
38
39
40
41
42
43
44
45
46
47
48
49
50
51
52
53
54
55
56
57
58
59
60

1   **THRESHOLD IDENTIFICATION FOR MICRO-TOMOGRAPHIC DAMAGE**

2   **CHARACTERIZATION IN A SHORT FIBRE REINFORCED POLYMER**

3

4   **Short running head: THRESHOLD IDENTIFICATION FOR MICRO-CT**

5   **DAMAGE CHARACTERIZATION IN A SFRP**

6   F. Cosmi[*], C. Ravalico

7   [a] *Università degli Studi di Trieste – Dipartimento di Ingegneria e Architettura,*

8   *Via A. Valerio 10, 34127 Trieste, e-mail: cosmi@units.it*

9   *Corresponding author. Tel.: +39 0405583431; fax: +39 0405583812.*

10   *E-mail address: cosmi@units.it (F. Cosmi).*

11   **Abstract**

12   The micro-tomographic technique represents an important tool for the analysis of the

13   internal structure in short fibre reinforced polymers samples. For the investigation of

14   damage mechanisms, detection of the micro-voids within the matrix can be facilitated

15   by applying a tensile load in-situ during the scan. The investigations here described

16   started from two micro-CT acquisitions, at different strain levels, of the same

17   PA6.6GF10 sample. An original procedure for micro-voids identification is proposed,

18   based on the statistical elaboration of the matrix grey-tones range. In order to validate

19   the suggested procedure beyond visual inspection, an independent method based on an

20   optimization approach, which puts to use the two available micro-tomographic sets, was

21   developed and applied. The effect of the tensile load, which can induce a progression of

22   the damage within the specimen, was investigated and the relations among strain, fibre

23   distribution and micro-voids volumetric fraction were studied. Our findings point out

24   that the mechanisms of damage progression, even under static loading as in this case,

25   appear to be more complex than those related to the fibre-density induced stress

26   concentrations alone and require further investigation.

1. INTRODUCTION

It is well known that the mechanical properties of short fibre reinforced polymers (SFRP), like stiffness and static or fatigue strength, strongly depend on fibre length and distribution, [1-8].

A quantitative evaluation of the micro-structure and of its effects on damage propagation is therefore required to develop accurate models to be used in the design of short fibre reinforced polymers.

Synchrotron radiation micro-computed tomography (micro-CT) is a high spatial resolution, non-destructive technique. It has been successfully used to characterize different types of defects like delamination, matrix cracking, and to detect micro-voids formation. It represents a promising tool for studying the processes of deformation and of failure of materials characterized by a complex micro-structure, where different damage mechanisms, not completely understood yet, act at different scales [9–28].

The presence of micro-voids inside polymer based materials can be detected if a tensile load is applied during the acquisitions, usually by means of a test-rig designed to be transparent to the X-rays in the region of the acquisition. In this paper, three typical aspects of this technique are discussed: (i) an original method based on the statistical elaboration of the matrix grey-tone distribution is proposed for micro-voids identification; (ii) the segmentation technique is validated by means of an independent method implementing an optimization approach and (iii) the effect of the applied load, which can possibly damage the sample and alter the micro-voids distribution during the micro-CT acquisitions, is investigated.

1   **2. EXPERIMENTAL PROCEDURE**

2   **2.1. Sample**

3   A PA6.6GF10 specimen of standard ASTM D1822 geometry, 9.6 mm^2 section, not

4   been previously loaded, was considered in this work, Fig.1a.

5   **2.2 Image acquisition**

6   The micro-tomographic technique starts from the acquisition of a large number of

7   radiographic projections of the sample, which is placed on a rotary table and positioned

8   at different angular positions with respect to the radiation source. In this work, 2400

9   projections for each tomographic scan were acquired over 360 ° at the SYRMEP

10   beamline of Elettra, the synchrotron radiation facility in Trieste, with a white beam and

11   at a source-detector distance of 10 cm.

12   The cross-sections (slices) of the sample structure were reconstructed from the angular

13   projections by means of the STPv4.04 software, developed in house at Elettra. A 3D

14   representation of the internal structure of the short fibres within reinforced polyamide

15   samples can then be obtained by stacking the slices and can be used as a starting point

16   for morphological and structural investigations [29-36].

17   The images used in this work have a 2.2 micron resolution. At this resolution, the

18   volume of data collected by examining even small portions of the sample is very large.

19   For each tomographic scan, the slices were reconstructed in 32 bits (45 MB each slice),

20   converted to 8 bits, rotated so that the sample axes were aligned with those of the

21   reconstructed images and cut to fit the sample dimensions, as in [37].

22   Even if the examined sample had not been loaded before, micro-voids were present

23   within injection-molded specimen, due to air trapped during the manufacturing process

24   and formation of volatiles during cure. As discussed in [37], since the polymer matrix

25   tends to close around the defects, a tensile test-rig must be used to highlight the micro-

26   voids in the micro-CT images. In this work, two different micro-CT scans of the

1   specimen were obtained in correspondence to the application of two low intensity strain

2   levels, ε_1 and ε_2, respectively:

3   -   Tomo_1, $\varepsilon_1 = 0.0013$, elongation between the clamps $\Delta L_1 = 0.063$ mm;

4   -   Tomo_2, $\varepsilon_2 = 0.0056$, elongation between the clamps $\Delta L_{65} = 0.271$ mm.

5   Fig. 1b shows the experimental stress-strain diagram, obtained from specimens of the

6   same batch on a servo-hydraulic Instron 8801-A2 machine with a 100kN load cell

7   directly recording the movements of the mobile grip at a crosshead speed of 1mm/s and

8   ambient conditions of 20°C, 60% humidity [38]. . The strain levels imposed during the

9   two tomographic scans Tomo_1 and Tomo_2 are also reported on the diagram.

10   A rectangular prism in the central part of the specimen (Fig.2a) was considered for the

11   analyses. The dimensions of the reconstructed volume in Tomo_1 are 2.7720 x 2.7720 x

12   3.4320 mm (corresponding to 1286 x 1286 pixel x 1560 slices), Fig. 2b. Analysis of the

13   sample morphology was also performed at a smaller scale by examining 4 sub-sets of

14   390 slices (0.854 mm), shown in Fig. 2c.

15   In order to be able to compare the two tomographic scans (Tomo_1 and Tomo_2) of the

16   same sample, an accurate identification of the homologous volumes required some

17   degree of attention and was performed manually by exploiting the presence of clearly

18   recognizable fibre aggregations, similarly to [33]. The relative position of the slices in

19   the two reconstructions was checked every 50 slices (0.1100 mm). The homologous

20   volume in Tomo_2 has the same square base of the volume identified in Tomo_1 (the

21   deformations in the *xy* plane were not examined) and has a slightly higher number of

22   slices in the *z*-direction: 1286 x 1286 pixels x 1568 slices corresponding to 2.7720 x

23   2.7720 x 3.4496 mm, due to the different elongation imposed on the specimen during

24   the scans. The four Tomo_2 sub-sets were identified in the same way, and different

25   elongations were registered in the different sub-sets.

26   **3. IMAGE ANALYSES**

1 The 8-bit images range of grey-tones is 0-255. The grey tones histogram of a

2 tomographic image results from radiation absorption in the different parts of the sample

3 and from possible phase contrast effects, which in this work we tried to avoid by

4 limiting the sample-detector distance during the scans. In our images, the glass fibre is

5 the highest absorbing phase and appears of light tone, micro-voids are virtually

6 transparent to the radiation and appear dark, while the polyamide matrix, of

7 intermediate absorption properties, occupies the central part of the histogram. Given the

8 low fibre content and the limited amount of damage, the matrix phase occupies the most

9 relevant part of both histograms, shown in Fig.3

10 The segmentation process consists in setting the threshold values that are most

11 appropriate for an unambiguous identification of the phases within the sample, in this

12 case fibre, matrix and micro-voids. In this work, original methods were developed for

13 the matrix/micro-voids segmentation and its validation.

14 **3.1. Identification of fibre**

15 Since the glass fibre fraction charging the sample is known, the fibre threshold can be

16 obtained by requiring that the fibre volumetric fraction (FV/TV) in the reconstructed

17 volume matches the fibre volumetric fraction imposed by the manufacturing process, as

18 suggested in [3]. In this work, a fiber fraction of 10% by weight corresponds to a 4.68%

19 volume fraction and to a threshold value of 106 and 108 for the Tomo_1 and the

20 Tomo_2 tomographic set respectively, so that the grey-tone values from 106 to 255 and

21 from 108 to 255 identify fiber in the two tomograms.

22 **3.2. Identification of matrix and micro-voids**

23 Specific methods and robust algorithms for micro-voids segmentation in micro-

24 tomographic images are required in the study of damage propagation mechanisms. The

25 original technique adopted in this work for the evaluation of the micro-voids threshold

1   is of general value and starts from the identification of the matrix grey-tones range and

2   their statistical elaboration.

3   The reconstructed volumes Tomo_1 and Tomo_2 were divided and examined in 16

4   stacks of 100 slices. A volume clearly made only of matrix, with no fibre and no micro-

5   voids, was selected in each one of the stacks. Each one of these matrix-only volumes

6   was 56x56 pixel in the *xy* plane and consisted of 5 slices (Fig.4) so that a total number

7   of 15,680 matrix-only voxels were available for each tomographic set. The mean (μ)

8   and the standard deviation (σ) of the matrix grey-tone distribution were computed for

9   each tomographic set, as reported in Table 1. The lower threshold value for the matrix

10   phase was selected at $\mu-3.5\sigma$, which in both sets corresponded to the first grey-tone

11   value with a minimum of 100 counts or more out of the 15,680 available.

12   It can be argued that, given the low percentage of fibre charge in this sample, the

13   selection of the matrix-only volumes was a relatively easy task. Nevertheless, the

14   method is of general value and can be easily extended for the analysis of samples that

15   are denser in fibre, for example by micro-CT scanning a small reference volume of

16   uncharged matrix together with the specimen.

17   A visual inspection, an example of which is shown in Fig. 5a, can provide a first

18   confirmation of the adopted threshold value. In Fig. 5b, the structures of fiber and

19   micro-voids are highlighted in a longitudinal section of the reconstructed sample,

20   depicting a situation in agreement with the model proposed by Horst and Spoormaker

21   [39], with a preferred localization of micro-voids at the fibre ends.

22   An original independent method, based on an optimization approach, was further

23   adopted to confirm these threshold values, as discussed in section 5.

24   **3.3 Morphological analyses**

6

1 Numerous methods have been proposed in literature in order to describe the

2 morphological properties of a two-phase material. The Mean Intercept Length, MIL, is a

3 global method that has been successfully applied to describe the fibre orientation in

4 SFRP from micro-CT scans [29-36]. The MIL is computed by superimposing a grid of

5 parallel lines in several 3D directions to the image of the reconstructed volume and by

6 dividing the length of the grid by the number of transitions in a same phase [40]. The

7 3D locus of the MIL measurements can be approximated by an ellipsoid and therefore

8 be described by a tensor. The eigenvectors correspond to the principal directions of the

9 anisotropic structure and the normalized eigenvalues, Hi, quantify the phase

10 organization along the principal directions. An Index pf Anisotropy can be defined:

11 IA = 1 - MIN (Hi) / MAX (Hi) (1)

12 where IA = 0 for perfect isotropy and IA = 1 at the other extreme.

13 The morphological analyses were carried out in Quant3D [41].

14 **4 RESULTS**

15 **4.1 Reconstructed specimen volume**

16 The strain increment imposed in the examined portion of the specimen between

17 Tomo_1 and Tomo_2 was 0.005, as computed from the number N of slices needed to

18 represent the two homologous volumes:

19 $$\varepsilon = \frac{L_f - L_i}{L_i} = \frac{N_{Tomo\_2} - N_{Tomo\_1}}{N_{Tomo\_1}} \qquad (1)$$

20 where L_i and L_f represent the length of the sample in the Tomo_1 and Tomo2

21 conditions respectively.

22 At the applied strain, the volume fraction of voids (VV/TV) increased from 5.065% in

23 Tomo_1 to 5.108% in Tomo_2.

24 The MIL rose diagrams of the fibre distributions in the reconstructed volumes of

25 Tomo_1 and Tomo_2 is shown in Fig.6. The plots clearly indicate that the fibre

7

1 orientations are primarily directed along the specimen longitudinal axis and that the

2 structure is transversely isotropic (the fibre orientation distribution is symmetric about

3 the principal direction). The fibre MIL Index of Anisotropy remains unchanged

4 (IA=0.57) between Tomo_1 and Tomo_2, demonstrating that the strain increase applied

5 between the two acquisitions does not alter the fibre distribution in the specimen.

6 As already mentioned, the volume fraction of micro-voids increases with the applied

7 strain, but this is not the only effect, since the micro-voids tend to elongate in the

8 loading direction, as evidenced by the shape of the MIL rose diagram, as shown in

9 Fig.7, and by the values of the Anisotropy Index in Tomo_1, IA = 0.63, and Tomo_2,

10 IA = 0.65.

11 **4.2 Reconstructed sub-sets**

12 In Fig.8, the fibre volumetric fraction in the four reconstructed sub-set (shown in Fig.2c)

13 is reported for the two tomographic sets. It can be noted that the FV/TV local value does

14 not change between the homologous sub-sets, thus confirming that the examined

15 volumes are homologous.

16 Strain in the 4 sub-sets, computed with (1), ranged from a lowest value of 0.0025 to a

17 highest value of 0.0076, as shown in Fig. 9.

18 Also the local micro-voids volumetric fraction (VV/TV) was recognized to vary among

19 the 4 sub-sets of each tomographic set, as shown in Fig. 10. It can be noted that the

20 maximum strain and the peak volumetric fractions of fibre and micro-voids were all

21 registered in the same sub-set.

22 As the applied strain increases between Tomo_1 and Tomo_2, the volume fraction of

23 voids (VV/TV) increases with similar trends in each examined subset, Fig.10. The

24 correlation coefficient between the subsets volume fraction of voids in Tomo_1 and in

25 Tomo_2 is high, $R^2 = 0.888$. At a local level, the micro-voids and the fibre volumetric

26 fractions in Tomo_1 appear to be strongly correlated, $R^2 = 0.924$. The correlation

1
2
3
4
5
6
7
8
9
10
11
12
13
14
15
16
17
18
19
20
21
22
23
24
25
26
27
28
29
30
31
32
33
34
35
36
37
38
39
40
41
42
43
44
45
46
47
48
49
50
51
52
53
54
55
56
57
58
59
60

1   between the micro-voids and the fibre volumetric fraction in Tomo_2 is less

2   pronounced, $R^2 = 0.710$. These results indicate that the initial micro-voids formation is

3   more likely to occur in areas of local higher fiber density, coherently to what observed

4   on a qualitative level in [25].

5   **5. VALIDATION OF THE MATRIX/MICRO-VOIDS THRESHOLD VALUE**

6   Starting with the two available micro-tomographic sets, it was possible to develop an

7   independent method for the validation of the threshold value for matrix and micro-voids

8   segmentation.

9   First of all, it must be considered that small variations in the beam parameters, which

10   are always possible between two different acquisitions, are reflected in this work by a

11   systematic difference of 2 grey-tones between all the corresponding thresholds found

12   for Tomo_1 and Tomo_2 sets, see Table 1. The validation procedure applied in this

13   work is based on an optimization approach and requires a single threshold value for the

14   two tomographic sets. The tonal range of Tomo_2 was therefore shifted of two values in

15   order to conform with that of Tomo_1. In this work, 17 pairs of homologous slices,

16   evenly distributed along the reconstructed specimen volume, were considered. The tonal

17   range shift had a negligible effect on the micro-voids distribution, since only a total of

18   20 pixels out of 28.114.532 were lost in the 17 slices. With this expedient, when a slice

19   in Tomo_1 is subtracted from the homologous one in Tomo_2 the difference between

20   the two images represents the micro-voids deformations, caused by the sample

21   elongation between the two scans (and the possible artifacts).

22   A second, straightforward, consideration is that any modification of the threshold value

23   has a contrasting result on the volume fractions of matrix and of voids respectively, i.e.

24   if the threshold value is lowered, the volume fraction of matrix increases and the

25   volume fraction of voids decreases. These aspects can be considered in an optimization

9

framework, and the problem of separating the micro-voids from the matrix can be seen

as the search for the best compromise.

A large number of multi-objective evolutionary algorithms have been proposed and

successfully applied [42–48]. Without going into the details of the mathematical and

implementation issues of the optimization strategy, it may suffice to cite that the

MOGA, Multi-Objective Genetic Algorithm including selection, crossover and

mutation, implemented in the modeFRONTIER [49] multi-objective tool, was adopted.

For the 17 homologous images, the histograms of Tomo_1, Tomo_2 and of the images

differences were used in input, and the conflicting, objective functions, or target goals,

were the contemporary maximization of the cumulative distributions of the grey-tones

corresponding to the matrix in Tomo_1 (Ob1) and in Tomo_2 (Ob2) and to the micro-

voids in the image differences (Ob3), as shown in the workflow outlined in Fig. 11.

Equal weights were imposed on the objective functions. The number of generations was

set to 1000, the probability of cross-over to 0.5, the probability of selection to 0.05 and

the probability of mutation to 0.05. The final result of the simulation is described by the

Pareto front, which represents the locus of points that tend to maximize the variables. In

this area, an improvement in one objective necessarily leads to a deterioration of the

other objectives. The optimal solution is usually chosen on the knee of the Pareto front.

The solution corresponding to the adopted threshold value is highlighted in Fig. 12,

confirming the effectiveness of the method described in Section 3.

6. DISCUSSION AND CONCLUSIONS

This paper examines some typical features of the application of the micro-tomographic

technique for the analysis of damage mechanisms in SFRP samples.

Two micro-CT scans of the same sample were acquired at different strain levels and the

elongations within the samples were computed from the number of slices needed to

represent the two homologous volumes in the two reconstructions. As expected with the

1 chosen specimen geometry and the local variations in fibre distribution, strain

2 distribution was not uniform along the Z axis. Micro-CT and Digital Volume

3 Correlation have recently been used to characterize the complex mechanical behavior of

4 heterogeneous and fibrous materials [51, 52]. This Our use of the reinforce fibres as

5 markers can be regarded as a first step towards the development of Digital Volume

6 Correlation (DVC) applications or specific 3D methods to estimate the displacements

7 and the strain field within the reconstructed volume of SFRP specimens, allowing new

8 insights on their behavior.

9 A general procedure for micro-voids identification in micro-CT analyses was proposed,

10 based on the identification and statistical elaboration of the matrix grey-tones range.

11 In order to validate the suggested procedure beyond visual inspection, an independent

12 method based on an optimization approach, which puts to use the two available micro-

13 tomographic sets, was developed.

14 Although it was recognized that clusters of fibres, resulting in an increased fibre

15 volumetric fraction at the local level, strongly facilitate the formation of micro-voids,

16 our findings point out that the mechanisms of damage progression, even under static

17 loading as in this case, appear to be more complex than those related to the fibre-density

18 induced stress concentrations alone and require further investigation.

19 Moreover, it was recognized that, although the fibre distribution for two small strain

20 values, located in the elastic range, is not altered by the load change, not only the

21 micro-voids volume fraction is increased, but also the micro-voids shape and

22 distribution are influenced. This observation leads to an important methodological

23 consequence. At present, the use of a test-rig to apply a tensile load during the

24 acquisitions appears to be essential for the detection of the micro-voids with the

25 tomographic technique. However, our findings show that the results obtained with this

26 procedure, for example in terms of micro-voids volumetric fraction, cannot be

1 considered as absolute values, but can only be used to compare specimens of the same

2 type and subjected to the same load.

3 Overall, even though the relationships observed between the distributions of micro-

4 voids, fibres and strain cannot be considered sufficient to express any general

5 conclusion on the behavior of short fibre reinforced composites and far more extended

6 analyses are under way, the results here discussed represent a step towards a more

7 extensive exploitation of the potential offered by the micro-tomographic analyses in the

8 study of the damage mechanisms of SFRP.

9 **ACKNOWLEDGEMENTS**

15 **REFERENCES**

16 [1]   B. Mouhmid B. et al.(2009) An experimental analysis of fracture mechanisms of

17 short glass fibre reinforced polyamide 6,6. DOI: 10.1016/j.compscitech.2009.07.003,

18 CSTE, 69, 2521–6.

19 [2]   Tiesong L. , Dechang J., Meirong W., Peigang H., Defu L. (2009) Effects of

20 fibre content on mechanical properties and fracture behaviour of short carbon fibre

21 reinforced geopolymer matrix composites. DOI 10.1007/s12034-009-0011-2 Bull

22 Mater Sci 32, 77–81.

23 [3]   Piment S. et al. (2010) Mechanical analysis and toughening mechanisms of a

24 multiphase recycled CFRP DOI: 10.1016/j.compscitech.2010.06.017. CSTE 70:1713–

25 25.

26 [4]   Schoßig M. et al. (2011) . ESEM investigations for assessment of damage

27 kinetics of short glass fibre reinforced thermoplastics – results of in situ tensile tests

28 coupled with Acoustic Emission Analysis. DOI: 10.1016/j.compscitech.2010.12.004

29 CSTE 71, 257–65.

1   [5]   Sul J.H., Prusty B.G., Ray T. (2011) Prediction of low cycle fatigue life of short

2   fibre composites at elevated temperatures using surrogate modelling. DOI:

3   10.1016/j.compositesb.2011.04.047 Compos B Eng 42(6), 1453–60.

4   [6]   Klimkeit B. et al. (2011)   Multiaxial fatigue life assessment for reinforced

5   polymers. DOI: 10.1016/j.ijfatigue.2010.12.004 Int J Fatigue 33(6), 766–80.

6   [7]   Saayama T., Okabe T., Aoyagi Y., Masaaki M. (2013) Prediction of failure

7   properties of injection-molded short glass fiber-reinforced polyamide 6,6. DOI:

8   10.1016/j.compositesa.2013.05.00 Composites Part A 52, 45-54.

9   [8]   Notta-Cuvier D., Lauro F., Bennani B., Balieu R. (2014). Damage of short -fibre

10 reinforced materials with anisotropy induced by complex fibres orientations. DOI:

11 10.1016/j.mechmat.2013.09.011 Mechanics of Materials 68, 193-206.

12 [9]   Buffière J.Y. et al. (2010) In situ experiments with x ray tomography: an

13 attractive tool for experimental mechanics DOI: 10.1007/s11340-010-9333-7. Exp

14 Mech;50, 289–305.

15 [10]   Cosmi F. et al. (2005). The X-ray tomography technique for fatigue cracks

16 reconstruction in Al 5083 specimen. Proc. Int Conf on Fracture and Damage Mechanics

17 IV, Mallorca (Spain).

18 [11]   Wang et al. (2005) High-pressure x-ray tomography microscope: Synchrotron

19 computed microtomography at high pressure and temperature. DOI: 10.1063/1.1979477

20 Rev. Sci. Instrum., 76.

21 [12]   Rivers M., Sutton S., Newville M. (2004) "Imaging in Earth", Planetary and

22 Environmental Science, Workshop on Emerging Scientific Opportunities using X-ray

23 Imaging, August 29-31.

24 [13]   Salvo L. et al. (2003) X-ray micro-tomography an attractive characterisation

25 technique in materials science. DOI: 10.1016/S0168-583X(02)01689-0 Nucl. Instr. and

26 Meth. in Phys. Res. B, 200, 273–286.

27 [14]   Toda H. et al. (2006) Quantitative Assessment of Microstructure and its Effects

28 on Compression Behavior of Aluminum Foams via High-Resolution Synchrotron X-

29 Ray Tomography. DOI: 10.1007/s11661-006-1072-0 Metallurgical and materials

30 Transactions A, 37(4), 1211-1219.

31 [15]   Bull D.J. et al. (2013) A comparison of multi-scale 3D X-ray tomographic

32 inspection techniques for assessing carbon fibre composite impact damage. DOI:

33 10.1016/j.compscitech.2012.12.0; CSTE 75, 55–61.

[16]   Schilling P.J. et al. (2005) X-ray computed microtomography of internal damage in fibre reinforced polymer matrix composites. DOI: 10.1016/j.compscitech.2005.05.014 CSTE 65, 2071–8.

[17]   Hodgkins A. et al. (2006) X-ray tomography observation of crack propagation in nuclear graphite. DOI: 10.1179/174328406X114126 Mater Sci Technol 22, 1045–51.

[18]   Breuni T.M., Kinney J.H., Stock S.R. (2006). MicroCT (microtomography) quantification of microstructure related to macroscopic behaviour: Part 2 – Damage in SiC–Al monofilament composites tested in monotonic tension and fatigue. DOI: 10.1179/174328406X114153 Mater Sci Technol; 22, 1059–67.

[19]   Awaja F. et al. (2011) The investigation of inner structural damage of UV and heat degraded polymer composites using X-ray micro CT. DOI: 10.1016/j.compositesa.2010.12.015 Compos. A 42, 408–18.

[20]   Tan K.T., Watanabe N., Iwahori Y. (2011). X-ray radiography and micro-computed tomography examination of damage characteristics in stitched composites subjected to impact loading. DOI: 10.1016/j.compositesb.2011.01.011 Compos. B 42, 874–84.

[21]   Tsukrov I. et al. (2012) Finite element modeling to predict cure-induced microcracking in three dimensional woven composites. DOI: 10.1007/s10704-011-9659-x Int J Fract 172(2), 209–16.

[22]   Little J.E., Yuan X., Jones M.I. (2012). Characterisation of voids in fibre reinforced composite materials. DOI: 10.1016/j.ndteint.2011.11.011 NDT&E Int 46, 122–7.

[23]   Crivelli D. et al. (2010).. Microstructural damage assessment of pultruded materials by synchrotron light tomography. In: Proc. of 27th Danubia Adria Symposium. Wroclaw, Poland

[24]   Arif M.F., Saintier N., Meraghni F., Fitoussi J., Chemisky Y., Robert G. (2014). Multiscale fatigue damage characterization in short glass fiber reinforced polyamide-66. DOI: 10.1016/j.compositesb.2014.01.019 Composite Part B 61, 55-65.

[25]   Arif M.F., Meraghni F., Chemisky Y., Despringre N., Robert G. (2014). In situ damage mechanisms investigation of PA66/GF 30 composite: Effect of Relative humidity. DOI: 10.1016/j.compositesb.2013.11.001 Composite Part B 58, 487-495.

[26]   Hu X., Wang L., Xu F., Xiao T., Zhang Z. (2014). In situ observations of fractures in short carbon fiber/epoxy composites. DOI: 10.1016/j.carbon.2013.10.007 Carbon 67 (10), 368-376.

1   [27]   Tang M., Gao B., Shi H(2013).. Influence of voids on the matrix of C/C

2   composite. Advances in the Astronautical Sciences 146 (5), 511-520.

3   [28]   Goidescu C., Welemane H., Garnier C., Fazzini M., Brault R., Peronnet E.,

4   Mistou S. (2013). Damage investigation in CFRP composites using full-field

5   measurement techniques: Combination of digital image stereo-correlation, infrared

6   thermography and X-ray tomography. DOI: 10.1016/j.compositesb.2012.11.016

7   Composites B 48 (5), 95-105.

8   [29]   Bernasconi A., Cosmi F., Dreossi D. (2008),. Local anisotropy analysis of

9   injection moulded fibre reinforced polymer composites. DOI:

10 10.1016/j.compscitech.2008.05.022 CSTE 68, 2574-2581.

11 [30]   Bernasconi A., Cosmi F., Zappa E. (2010). Combined effect of notches and fibre

12 orientation on fatigue behavior of short fiber reinforced polyamide. DOI:

13 10.1111/j.1475-1305.2009.00667.x Strain 46, 435–45.

14 [31]   Cosmi F., Bernasconi A. (2010). Elasticity of short fibre reinforced polyamide:

15 morphological and numerical analysis of fibre orientation effects. Materiálové

16 ininierstvo, XVII, 6-10.

17 [32]   Cosmi F. (2011). A micro-mechanical model of the elastic properties of a short

18 fibre reinforced polyamide. DOI: 10.1016/j.proeng.2011.04.353 Procedia engineering,

19 2135-2140.

20 [33]   Cosmi F., Bernasconi A., Sodini N. (2011). Phase contrast micro-tomography

21 and morphological analysis of a short carbon fibre reinforced polyamide. DOI:

22 10.1016/j.compscitech.2010.09.016 CSTE 71, 23-30.

23 [34]   Cosmi F. (2011). Local Anisotropy and Elastic Properties in a Short Glass Fibre

24 Reinforced Polymer Composite. DOI: 10.1111/j.1475-1305.2009.00670.x Strain, 47,

25 215-221.

26 [35]   Bernasconi A., Cosmi F (2011). Analysis of the dependence of the tensile

27 behavior of a short fibre reinforced polyamide upon fibre volume fraction, length and

28 orientation. DOI: 10.1016/j.proeng.2011.04.352 Procedia engineering 2129-2134.

29 [36]   Bernasconi A., Cosmi F., Hine P.J (2012) Analysis of fibre orientation

30 distribution in short fibre reinforced polymers: a comparison between optical and

31 tomographic methods. DOI: 10.1016/j.compscitech.2012.08.018 CSTE 72, 2002-2008

32 [37]   Cosmi F., Bernasconi A. (2013). Micro-CT investigation on fatigue damage

33 evolution in short fibre reinforced polymers. DOI: 10.1016/j.compscitech.2013.02.008

34 CSTE 79, 70-76.

[38] Bernasconi A., Cosmi F., Taylor D. (2014). Analysis of the fatigue properties of different specimens of A 10% by weight short glass fibre reinforced polyamide 6.6, POTE DOI: 10.1016/j.polymertesting.2014.08.017.

[39] Horst J.J., Spoormaker J.L(1997).. Fatigue fracture mechanisms and fractography of short-glass-fiber-reinforced polyamide 6. Journal of Materials Science 32, 3641-3651.

[40] Odgaard A. (1997). Three-dimensional methods for quantification of cancellous bone architecture. DOI: 10.1016/S8756-3282(97)00007-0 Bone 4, 315–28.

[41] Ketcham R.A., Ryan T.M. (2004). Quantification and visualization of anisotropy in trabecular bone. DOI: 10.1111/j.1365-2818.2004.01277.x J Microsc. 213, 158–71.

[42] Coello C.A., Van Veldhuizen D. A., Lamont G. B. (2007), Evolutionary algorithms for solving multiobjective problems, Springer Verlag, New York, USA 2nd edition.

[43] Deb K. (2001). Multi-objective optimization using evolutionary algorithms, John-Wiley, Chichester

[44] Fonseca C.M., Fleming P. J (1993). Genetic algorithm for multiobjective otpimization: formulation, discussion and generalization. In Proceedings of the Fifth International Conference on Genetic algorithm (Ed. S. Forrest), Morgan Kauffamn, San Mateo, CA 416–423.

[45] Horn J., Nafploitis N., Goldberg D. E.. (1994) A Niched Pareto genetic algorithm for multiobjective optimization. In Proceedings of the First IEEE Conference on Evolutionary computation (Ed. Z. Michalewicz), IEEE Press, Piscataway, NJ, 98–105.

[46] Srinivas N., Deb K. (1995) Multiobjective function optimization using non dominated sorting genetic algorithm. IEEE Trans. Evol. Comput., , 2(3), 221–248.

[47] Rosic B., Rasuo B (2008),Application of multi-objective genetic algorithm to optimum design problems. In Proceedings of the First Symposium in MS Design, Bertinoro, Italy 17–18.

[48] Cosmi F., Muscia R. (1999). Ottimizzazione multiobiettivo di cambi di velocità per uso automobilistico: porgettazione preliminare del gruppo ingranaggi sincronizzatori- alberi. In Proceedings of the XXVIII AIAS Conference, Vicenza, Italy 445–458 (Italian).

[49] http://www.esteco.com/modefrontier accessed July 31, 2014

16

1   [50]   Cowin S.C. (1985). The relationship between the elasticity tensor and the fabric

2   tensor. Mech Mater. 4, 137–47.

3   [51] R. Brault et al. (2013), In-situ Analysis of Laminated Composite Materials by X-

4   ray Micro-Computed Tomography and Digital Volume Correlation. Experimental

5   Mechanics 53, 1143–1151.

6   [52] H. Tran et al. (2013). 3D mechanical analysis of low-density wood-based

7   fiberboards by X-ray microcomputed tomography and Digital Volume Correlation.

8   Mater Sci 48, 3198–3212.

For Peer Review

17

TABLES

Table 1: Mean and standard deviation of the matrix phase in the selected matrix-only volumes and thresholds for the phase identification in the two tomographic sets.

	μ (matrix-only)	σ (matrix-only)	Micro-voids thresholds	Matrix thresholds	Fiber thresholds
Tomo_1	87.5	3	0-76	77-105	106-255
Tomo_2	89.5	3	0-78	79-107	108-255

Figure 1: (a) Geometry of the standard ASTM D1822 specimen, and (b) stress-strain diagram from 4 specimens of the same batch. The strain levels imposed during the two tomographic acquisitions Tomo_1 and Tomo_2 are also reported.
175x69mm (300 x 300 DPI)
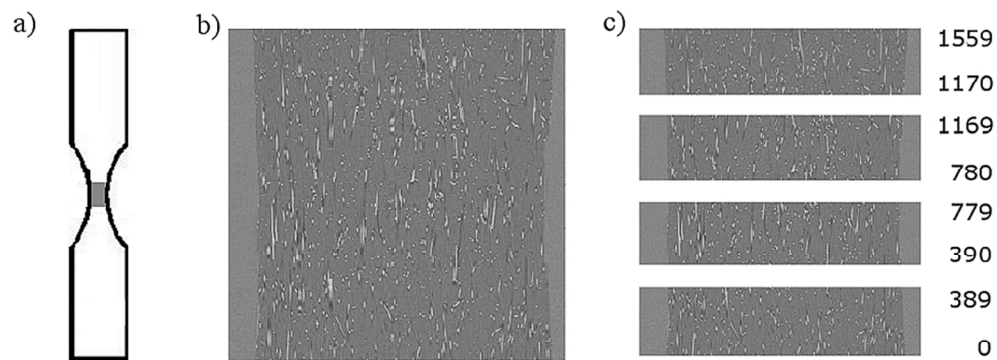
(Figure 2: (a) Selection of the acquired volume in the central part of the specimen, (b) longitudinal view of the reconstructed specimen volume in Tomo_1, 1286 x 1286 pixel x 1560 slices, (c) identification of the 4 examined sub-sets of 390 slices.
82x35mm (300 x 300 DPI)
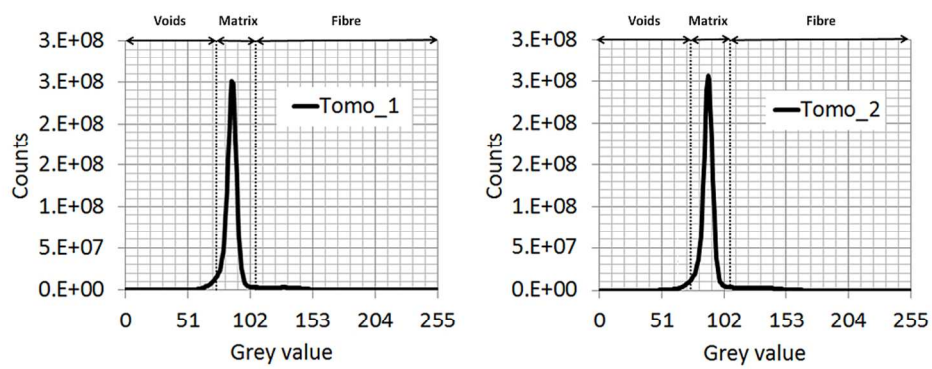
Figure 3: Histograms of the tomographic scans.
95x41mm (300 x 300 DPI)
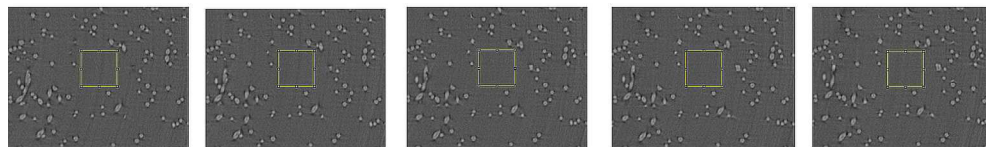
Figure 4: An example of matrix-only volume selection in the homologous regions of 5 successive slices, Tomo_1.
175x27mm (300 x 300 DPI)
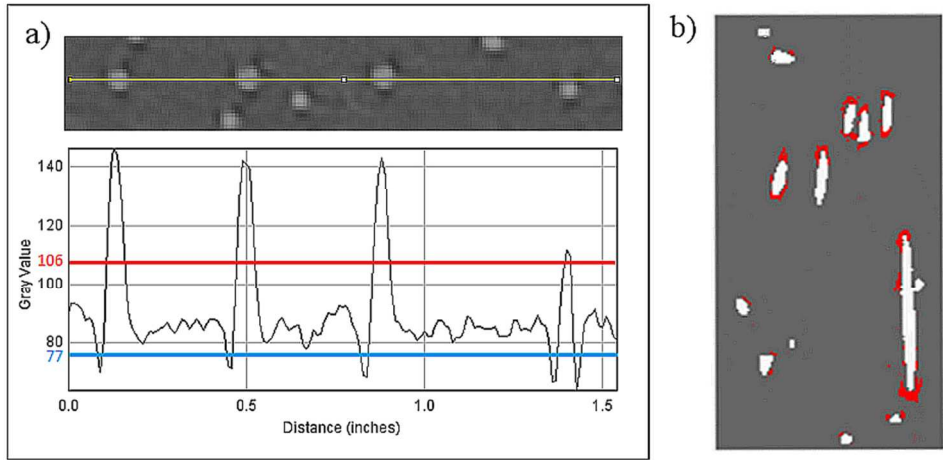
Figure 5: (a) Detail of the slice 999, Tomo_1 (above) and grey-tone plot along the yellow line, with indication of the threshold values (below); (b) zoom of a segmented longitudinal section, slices 799 to 1298, Tomo_1, where the fibres are depicted in white, the matrix is shown grey and the micro-voids are highlighted in red.
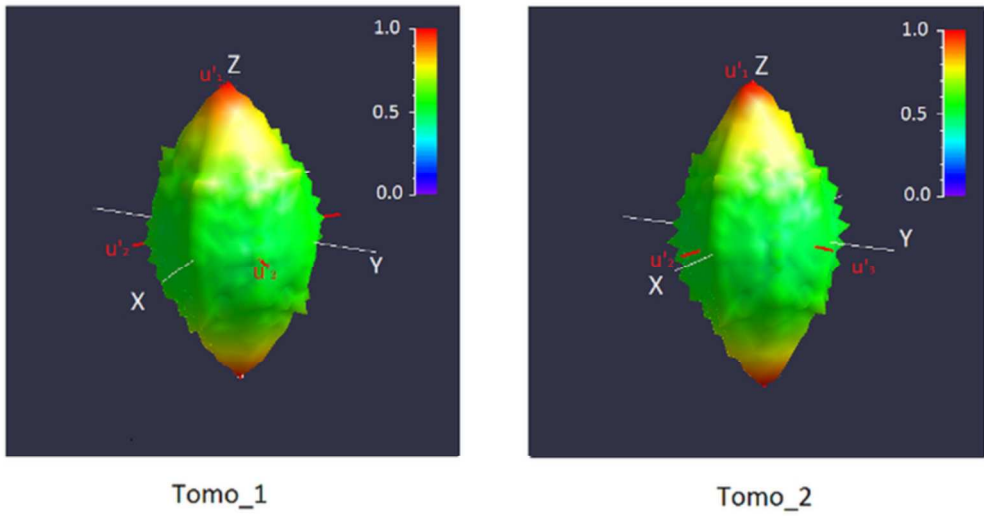82x41mm (300 x 300 DPI)
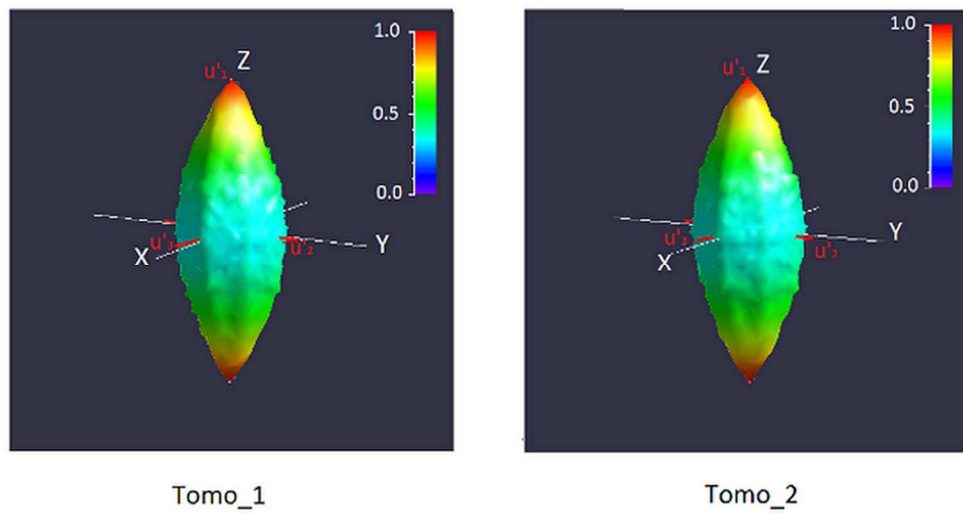
Figure 6: MIL rose diagrams of the fibre distributions in the reconstructed volumes of Tomo_1 and Tomo_2.
82x45mm (300 x 300 DPI)

1
2
3
4
5
6
7
8
9
10
11
12
13
14
15
16
17
18
19
20
21
22
23
24
25
26
27
28
29
30
31
32
33
34
35
36
37
38
39
40
41
42
43
44
45
46
47
48
49
50
51
52
53
54
55
56
57
58
59
60

Figure 7: MIL rose diagrams of the micro-voids distributions in the reconstructed volumes of Tomo_1 and Tomo_2.
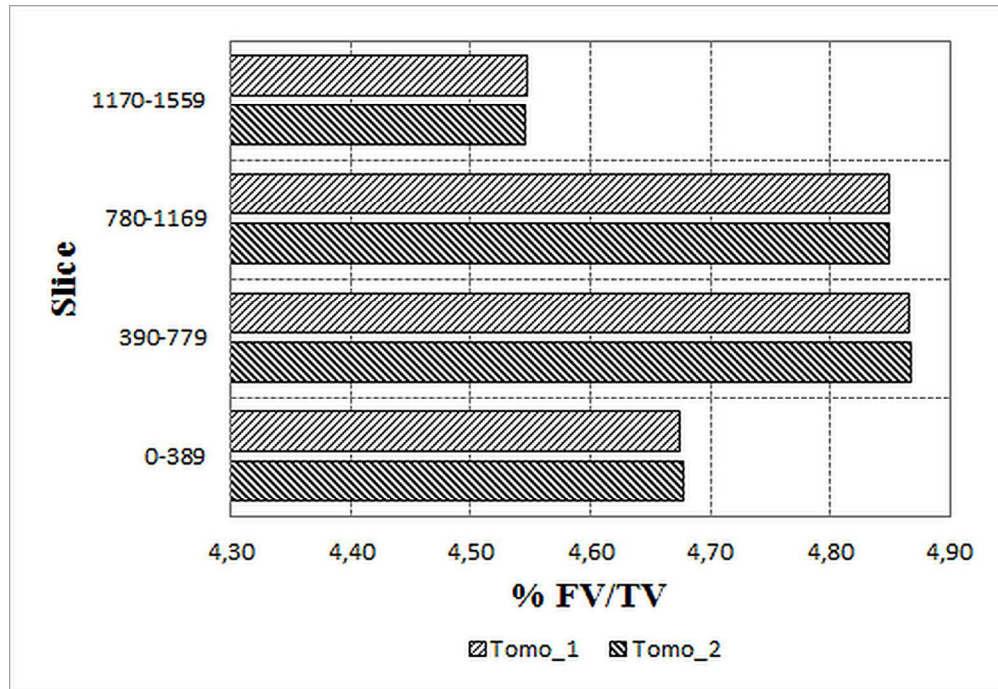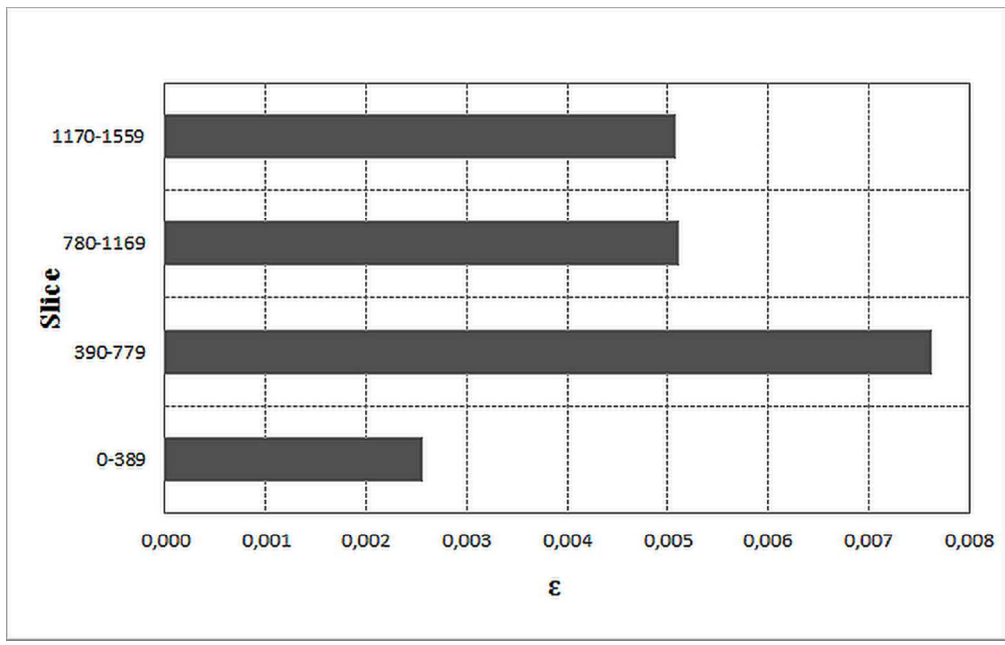82x47mm (300 x 300 DPI)

Figure 8: Local distribution of the fibre volumetric fraction (FV/TV) in the reconstructed sub-sets.
82x57mm (300 x 300 DPI)

1
2
3
4
5
6
7
8
9
10
11
12
13
14
15
16
17
18
19
20
21
22
23
24
25
26
27

Figure 9: Local distribution of strain (ε) in the reconstructed sub-sets.
82x52mm (300 x 300 DPI)

28
29
30
31
32
33
34
35
36
37
38
39
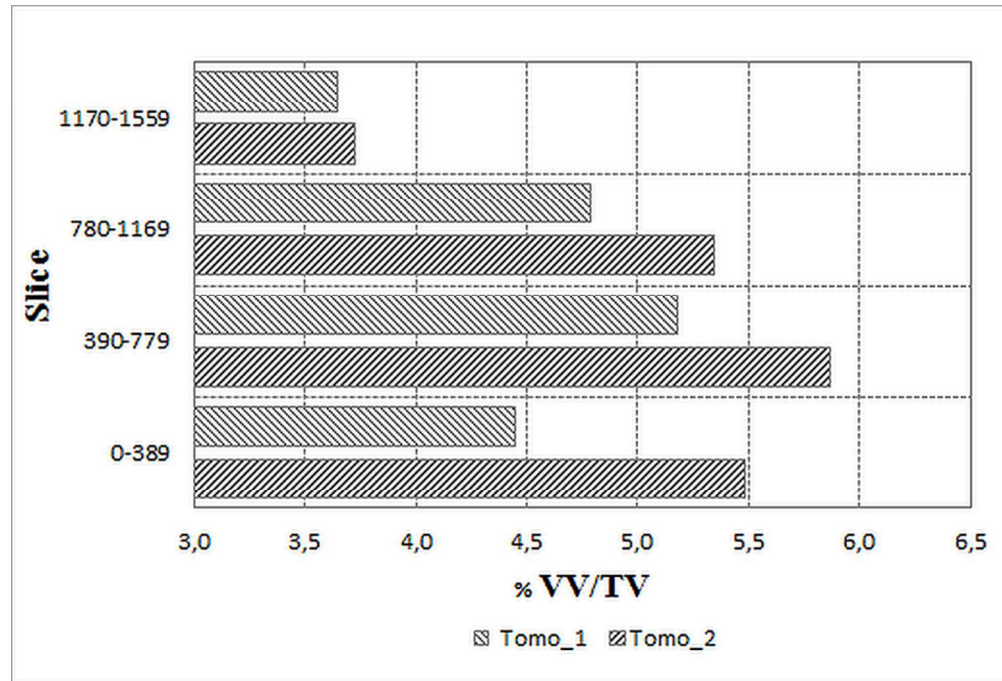40
41
42
43
44
45
46
47
48
49
50
51
52
53
54
55
56
57
58
59
60

Figure 10: Local distribution of the micro-voids volumetric fraction (VV/TV) in the reconstructed sub-sets.
82x56mm (300 x 300 DPI)

1
2
3
4
5
6
7
8
9
10
11
12
13
14
15
16
17
18
19
20
21
22
23
24
25
26
27
28
29
30
31
32
33
34
35
36
37
38
39
40
41
42
43
44
45
46
47
48
49
50
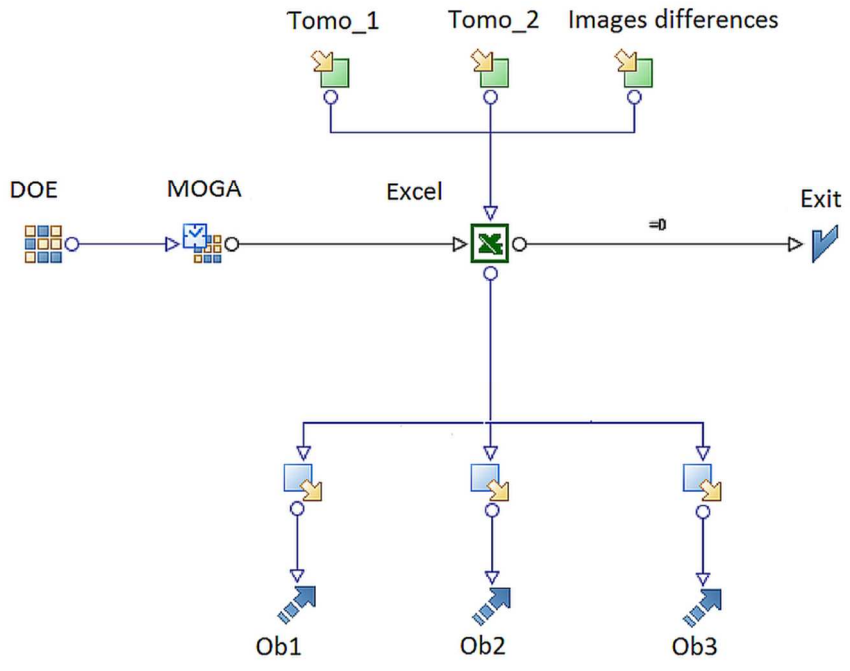51
52
53
54
55
56
57
58
59
60

Figure 11: ModeFRONTIER workflow. The target goals are the contemporary maximization of the cumulative distributions of the grey-tones corresponding to the matrix in Tomo_1 (Ob1) and in Tomo_2 (Ob2) and to the micro-voids in the image differences (Ob3).
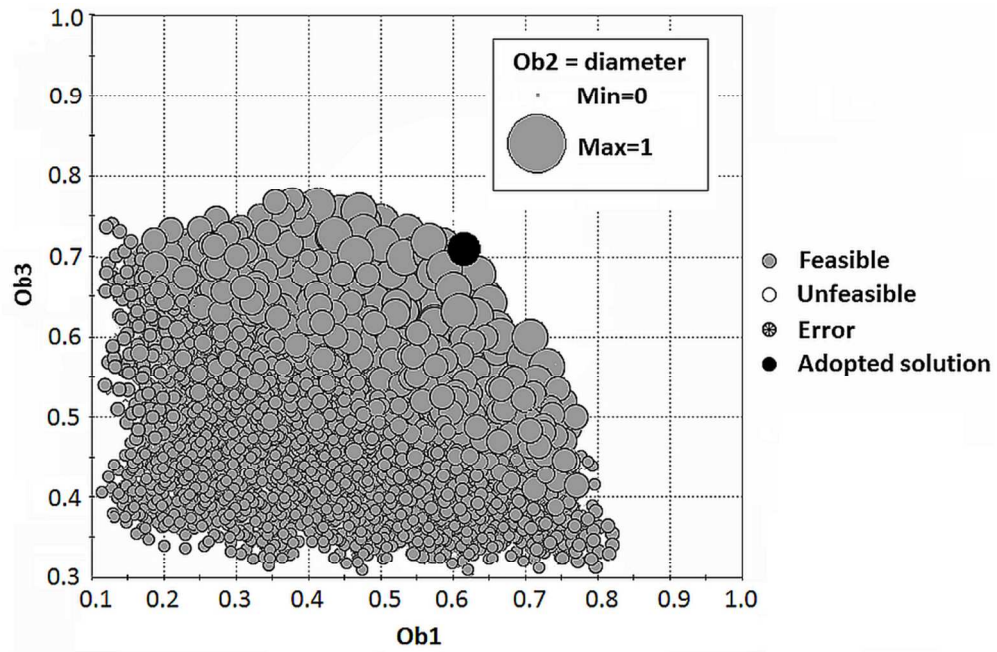82x64mm (300 x 300 DPI)

1
2
3
4
5
6
7
8
9
10
11
12
13
14
15
16
17
18
19
20
21
22
23
24
25
26
27
28
29
30
31
32
33
34
35
36
37
38
39
40
41
42
43
44
45
46
47
48
49
50
51
52
53
54
55
56
57
58
59
60

Figure 12: Pareto front resulting from the MOGA modeFRONTIER simulation. The solution adopted is highlighted.
82x54mm (300 x 300 DPI)